ARMA 22–0466

Characterization of fracture process zone in short beam compression tests on Barre granite

Garg, Prasoon
Colorado School of Mines, Golden, Colorado, USA
Hedayat, Ahmadreza
Colorado School of Mines, Golden, Colorado, USA
Griffiths, D.V.
Colorado School of Mines, Golden, Colorado, USA

This paper was prepared for presentation at the 56th U.S. Rock Mechanics/Geomechanics Symposium held in Santa Fe, New Mexico, USA, 26-29 June 2022. This paper was selected for presentation at the symposium by an ARMA Technical Program Committee based on a technical and critical review of the paper by a minimum of two technical reviewers. The material, as presented, does not necessarily reflect any position of ARMA, its officers, or members. Electronic reproduction, distribution, or storage of any part of this paper for commercial purposes without the written consent of ARMA is prohibited. Permission to reproduce in print is restricted to an abstract of not more than 200 words; illustrations may not be copied. The abstract must contain conspicuous acknowledgement of where and by whom the paper was presented.

ABSTRACT: Due to rock mass being commonly subjected to compressive or shear loading, the mode II fracture toughness is an important material parameter for rocks. Fracturing in rocks is governed by the behavior of a nonlinear region surrounding the crack tip called the fracture process zone (FPZ). However, the characteristics of mode II fracture are still determined based on the linear elastic fracture mechanics (LEFM), which assumes that a pure mode II loading results in a pure mode II fracture. In this study, the FPZ development in Barre granite specimens under mode II loading was investigated using the short beam compression (SBC) test. Additionally, the influence of lateral confinement on various characteristics of mode II fracture was studied. The experimental setup included the simultaneous monitoring of surface deformation using the two-dimensional digital image correlation technique (2D-DIC) to identify fracture mode and characterize the FPZ evolution in Barre granite specimens. The 2D-DIC analysis showed a dominant mixed-mode I/II fracture in the ligament between two notches, irrespective of confinement level on the SBC specimens. The influence of confinement on the SBC specimens was assessed by analyzing the evolution of crack displacement and changes in value of mode II fracture toughness. Larger levels of damage in confined specimens were observed prior to the failure than the unconfined specimens, indicating an increase in the fracture resistance and therefore mode II fracture toughness with the confining stress.

1. INTRODUCTION

The fracturing in laboratory-scale rock specimens is often characterized by the deformation of the inelastic region surrounding the crack tips, also known as the fracture process zone (FPZ) (Backers et al., 2005; Ghamgosar and Erarslan, 2016). While the influence of the FPZ on mode I fracture in rocks has been extensively investigated, there are limited studies on FPZ development in rocks under pure mode II loading (Ji et al., 2016; Lin et al., 2020; Garg et al., 2021; Li et al., 2021).

Over the years, various geometries such as anti-symmetric four-point bending (ASFPB) (Wang et al., 2016), cracked straight-through Brazilian disc (CSTBD) (Ayatollahi and Sistaninia, 2011), the double-edge semicircular bend (SCB) with an inclined notch (Aliha et al., 2006), short beam in compression (SBC) (Ko and Kemeny, 2007) and punch-through shear (PTS) (Backers et al., 2002) have been used to estimate mode II fracture toughness in rocks. The geometries mentioned above can be divided into two categories, namely: a) pure shear loading (i.e. $k_I = 0$) and b) compression-induced shear loading (i.e. $k_I < 0$) (Lui et al., 2018; Bahrami et al., 2020). The geometries from the first categories, such as notch deep beam (NDB) and semicircular bend (SCB) specimen with an inclined notch, typically result in the formation of a kink fracture (Ji et al., 2016; Lin et al., 2020; Garg et al., 2021). These geometries are selected based on the linear elastic fracture mechanics (LEFM), which assume that pure mode II loading is equivalent to pure mode II fracture (Ayatollahi and Sistaninia, 2011; Mirsayar et al., 2018; Bahrami et al., 2020). However, recent studies (Ji et al., 2016; Lin et al., 2020, 2019; Garg et al., 2021) based on characterization of the FPZ evolution under pure mode II loading have found that the pure mode II cracks are difficult to create in rocks without the elimination of the tensile stresses at the crack tip. For instance, Garg et al. (2021) tested various configurations of notch deep beam (NDB) specimens of Barre granite specimens and only found mode I fracture in these specimen geometries, despite the fact that these NDB specimens were subjected to the pure mode II loading condition.

The geometries based on compression-induced mode II loading such as short beam in compression (SBC), punch-through shear (PTS), and short core in compression

(SCC) tests, typically result in the formation of fracture in the original notches plane or along the maximum shear stress directions (Xu et al., 2020; Backers et al., 2002). In these geometries confining pressure can be applied to suppress tensile stresses at the notch tip and prevent crack kinking (Bahrami et al., 2020; Xu et al., 2020). In recent years, these compression-induced shear loading based geometries have been increasingly used to characterize the mode II fracture toughness in various rocks such as Aue granite, Carrara marble, Flagstaff sandstone, Escabrosa limestone (Backers, 2004; Ko and Kemeny, 2007; Jung et al., 2016; Li et al., 2021). Despite these applications, deformation behavior and fracture characteristics during the formation of mode II crack are not well understood. Additionally, only limited studies have explored the influence of mode II loading on the FPZ development in rocks (Backers, 2004; Lin et al., 2018), which typically requires a detailed analysis of the FPZ characteristics such as its shape and size, and magnitude of crack displacements. Optical techniques such as digital image correlation (DIC) can be a vital tool to characterize the FPZ development as it provides direct measurements of the displacement and strain fields inside the FPZ. Because of its simple setup and accurate measurements, DIC has gained attention in experimental fracture mechanics (Hedayat et al., 2014; Miao et al., 2018; Sharafisafa et al., 2018; Zhang et al., 2018).

The main aim of this study is to characterize the FPZ development in rock using geometries based on compression-induced mode II loading. For this purpose, the short beam compression (SBC) tests were performed on granite specimens. The SBC test was selected due to its numerous advantages over other cylindrical geometries such as ease of preparation and availability of multiple specimen configurations for pure mode II loading by changing ligament length (Ko, 2008). Unlike typical mode II tests such as punch-through shear tests, the SBC specimens, due to the planar surface, allow the estimation of surface deformation (using an optical technique such as DIC). This facilitates the estimation of various fracture properties such as crack displacements and fracture geometry. The SBC specimens of Barre granite were tested under compression loading along with the simultaneous implementation of 2D-DIC to characterize the various crack characteristics such as the FPZ evolution and its crack type under mode II loading. The fracture mode was determined based on both displacement and strain approaches of 2D-DIC. Additionally, the influence of confinement on the SBC specimens was assessed in terms of variation in mode II toughness and changes in characteristics of the developed FPZ.

2. SBC CONFIGURATION FOR PURE MODE II LOADING

The SBC specimen is a prismatic specimen with two horizontal notches under compression loading (Figure 1a). The pure mode II loading is achieved by creating two parallel and opposite notches, resulting in shear stress concentration at the central part of the specimen (Watkins and Liu, 1985). Both notches have a length of $a = W/2$ (W is specimen width) and are separated by a rock bridge length of c. Mode II stress intensity factor (K_{II}) for the SBC specimen (Watkins and Liu, 1985) can be defined using the following equations:

$$Y_{II}\left(\frac{c}{L}\right) = \frac{K_{II}}{\tau_f\sqrt{\pi a}} \tag{1a}$$

$$\tau_f = \frac{P}{cB} \tag{1b}$$

where P is the applied load on the specimen, L is specimen height, B is the specimen thickness, Y_{II} is the mode II non-dimensional geometrical factor, a is the notch length, and τ_f is nominal shear stress at the peak load and typically represents the average shear stress applied on the rock bridge between two horizontal notches. The geometrical factor (Y_{II}) primarily depends on the bridge length to height ratio (c/L).

Various experimental studies (Ko, 2008; Ko and Jeon, 2017) have shown the formation of the vertical crack, which is perpendicular to the notch plane in the SBC testing configurations. Therefore, estimation of mode II geometrical factor (Y_{II}) should account for the existence of crack tip perpendicular to the notch plane based on fracture mechanics theory. Xu et al. (2020) have shown that the addition of cracks tips along the shear crack direction in a short core compression test (similar to mode II testing configuration as SBC specimens) allows an accurate estimation of mode II stress intensity factors in rocks specimens. For this purpose, two shear cracks of the length of h_c along with horizontal notches were modeled in the finite element package ABAQUS (see inset in Figure 1). The small shear cracks are modeled as line cracks based on the assumption of LEFM with singular 6-node quadratic plane stress triangle elements (CPS6). These elements facilitate the calculation of stress intensity factors by replicating singularities at the crack tips. For accurate estimation of stress intensity, 20 rings of quadrilateral elements (20 elements for each ring) around crack tips were meshed using the sweep technique (Figure 1). The remaining region was modeled using the 8-node biquadratic plane stress quadrilateral elements (CPS8). The modeled SBC specimen had the same nominal dimensions as the experiments with two rectangular notches (Figures 1).

To model uniaxial compressive loading on the SBC specimen, a vertical displacement rate of 0.1 mm/step (1step =1sec) was applied at the top of the beam. The material behavior was assumed to be linearly elastic with Young's modulus (E) of 52 GPa and Poisson's ratio (v) of 0.16 to represent the elastic properties of Barre granite ported by Shirole et al. (2020). In the current study, the SBC specimens with (c/L) ratio of 0.2 were used as they are typically considered the most favorable configuration for the formation of the shear crack between two notches (Ko and Kemeny, 2007). Figure 2 shows the approximate linear variation of the numerical mode II stress intensity factor (K_{II}^{num}) at the shear crack tips with respect to normalized shear cracks length ($2h_c/c$) in the modeled specimens. Since actual SBC test specimens don't have shear cracks, the accurate estimation of mode II stress intensity factor (K_{II}) would require shear cracks in small lengths. However, FEM-based analysis cannot provide accurate results for small shear cracks as finite elements in the tip region require very dense meshing (element size < 0.001 mm). Therefore, the estimation of the mode II stress intensity factor (K_{II}) for the SBC specimens was done using extrapolation from the fitted curve of numerical mode II factor (K_{II}^{num}) vs. normalized shear cracks length ($2h_c/c$) (Figure 2). This extrapolation approach is valid since it follows the assumptions of LFEM and is known to provide a good estimate of the mode II stress intensity factor (K_{II}) in SBC type configurations (Ko and Kemeny, 2007, Xu et al., 2020). For a given bridge length to height ratio (c/L), mode II geometrical factor (Y_{II}) is then obtained using Eq 1a-b and numerical model.

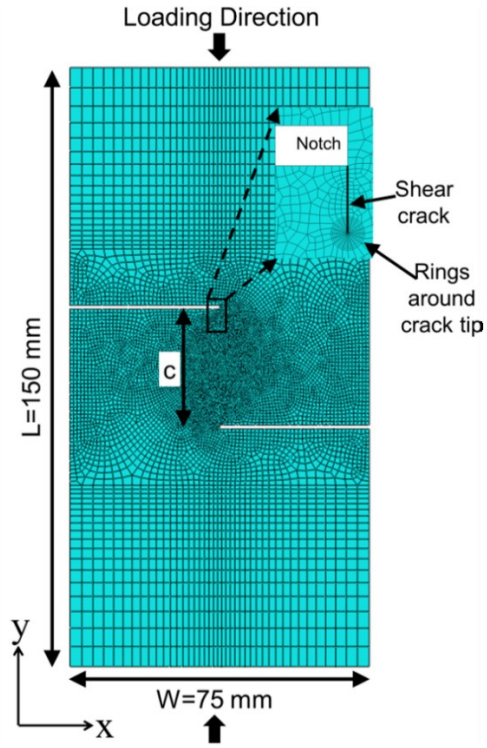

Figure 1. Finite element mesh used for estimation of geometrical factors in SBC specimens.

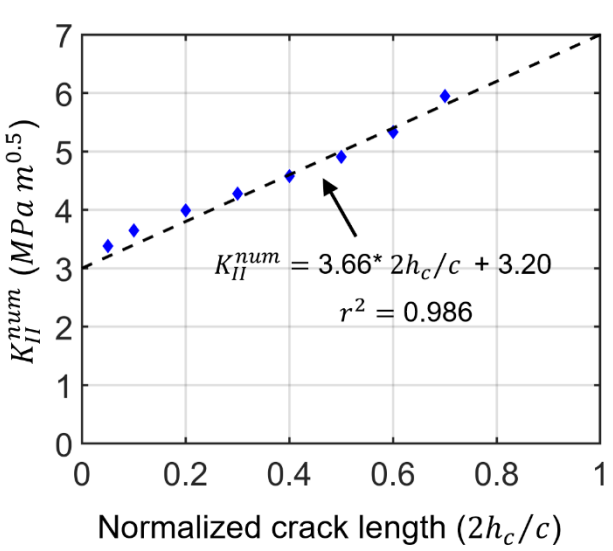

Figure 2. Variations of numerical mode II stress intensity factor (K_{II}^{num}) with respect to normalized shear crack length ($2\,h_c/c$) for the modeled SBC specimens with c/H of 0.2.

3. EXPERIMENTAL DESIGN

3.1 Specimen Preparation

This study characterizes the fracture processes in Barre granite specimens under pure mode II loading. Barre granite (B.G.) is a medium-grained crystalline rock with an average grain size of 0.87 mm (Shirole et al., 2020). The prismatic specimens of length L=150 mm, width W=75 mm, and thickness B=25 mm (Figures 1) were prepared from a large block of Barre granite. Two horizontal center notches with 1.02 mm aperture and 38 mm notch length was created by the Colorado WaterJet Company (Figure 1).

3.2 Experimental Setup and Testing

The SBC specimens of Barre granite were tested under compression loading using a biaxial loading device (Figure 3). The designed configuration for the experimental setup essentially consisted of two independent parts: (a) the horizontal loading frame to apply and control the required confinement on the specimen, and (b) the MTS loading machine to apply the uniaxial loading in the vertical direction (Figure 3). The horizontal loading frame consists of three main plates connected by four high-strength rods (Figure 3). The two outer plates with four rods provided the primary support for the flat jack and rock assembly placement, while the middle plate applied the load to the specimen (Figure 3). The hydraulic flat jack was used to apply the confinement in the horizontal direction, controlled through a hand-held hydraulic pump (Figure 3). The Teflon sheets in conjunction with elastic rubber were placed on two lateral surfaces of the specimen (Figure 3) in order to minimize the friction between the steel plates and rock specimen. The rubber sheets ensured a uniform stress distribution on

the lateral surfaces in an irregular-ended rock specimen. A steel spacer (dimensions of 50 mm x 72 mm x 25 mm) on the top of the specimen was used to transfer the axial load from the platens of the MTS machine to the specimen (Figure 3).

A small seating load was applied in the axial direction to securely fix the setup before starting the test. Subsequently, both confining pressure and axial load were increased in 0.2 MPa increments until the desired level of confinement was achieved. Finally, the axial load was increased at a constant rate of 0.1 µm/sec until specimen failure. The confining pressure (σ_c) acts normal to the future fracture plane, which typically forms in the rock bridge between two notches (Figures 1 and 3). The surface deformation was simultaneously monitored during testing using the 2D-DIC system, as shown in Figure 1. The DIC system consists of a CCD (Charged-coupled device) camera and two steady white sources (Figure 3). The post-processing of acquired images was done using Correlated Solutions software (VIC-2D) to measure the deformation and strain fields on the specimen's surface. The procedure involved first defining a region of interest (ROI) which is around 40×75 mm^2 in SBC specimens. Three input parameters, namely (a) subset size, (b) step size, and (c) filter size, were required for accurate estimation of the strain field around FPZs. The optimum values of each parameter are based on the suggestion by the author's earlier work (Garg et al., 2020 and 2021).

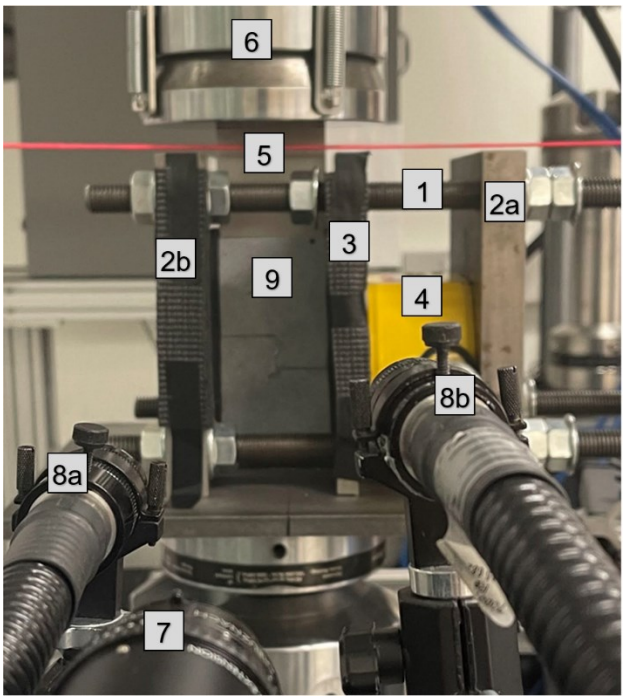

Figure 3. The experimental setup used in SBC test on prismatic specimen along with 2D-DIC where: (1) Steel rods (2) main support plates (3) middle plate (4) Hydraulic flat jack (5) Steel Spacer; (6) top platen of MTS machine; (7) CCD camera; (8) two light sources (9) Speckled specimen.

4. EXPERIMENTAL RESULTS

4.1 Fracture toughness evaluation

In each experiment, the axial load, the axial displacement, and the confining pressure values were recorded and then used along with the mode II geometrical factor (obtained from FEM-based analysis in Figure 2) to calculate the mode II fracture toughness of the SBC specimens under various levels of confining pressure. Figure 4 shows a linear variation of mode II fracture toughness (K_{II}) with confining pressure for the tested range. This linear increase in mode II fracture toughness at low confinement (σ_c < 30 MPa) agrees with the observation of other studies (Backers et al., 2002; Ko and Kemeny, 2007) on various rock types such as Aue granite, Carrara marble, Flagstaff sandstone. For instance, Ko and Kemeny (2007) found a linear variation in mode II fracture toughness (K_{II} =1.31-9.11 MPa mm$^{0.5}$) for Flagstaff sandstone with the confining pressures ranging from 0-10 MPa. Table 1 summarizes the results of SBC specimens at various levels of pressure (σ_c =0, 1.7, 3.5, 10.4 MPa). In this study, the SBC specimens were labeled as "SBC-σ_c-N" where "σ_c" represents confinement level, and "N" represents specimen number for a given confinement level "σ_c".

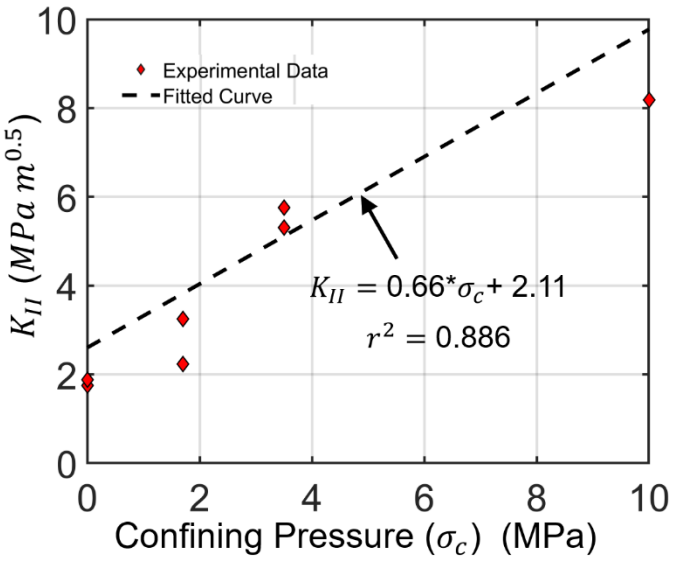

Figure 4. Variation of the mode II fracture toughness with respect to confining pressure.

Table 2: Experimental results of the SBC specimens of Barre granite tested in this study

Specimen No	Confining Pressure σ_c (MPa)	Peak load (kN)	K_{II} (MPa m$^{0.5}$)	w_{ne}^n (µm)	w_{ne}^s (µm)
SBC-0-1	0	11.2	1.75	3	3

SBC-0-2	0	12.0	1.88	5.2	5
SBC-1.7-1	1.7	20.7	3.25	40	42
SBC-1.7-2	1.7	14.2	2.23	47	51
SBC-3.5-1	3.5	36.8	5.76	95	109
SBC-3.5-2	3.5	33.9	5.31	98	114
SBC-10-1	10	52.2	8.18	134	130

4.2 Fracture characterization using DIC

Both strain and displacement approaches of the 2D-DIC were used to characterize the fracture development in SBC specimens tested under various confinement levels. Figures 5a-d present the contours of the minimum principal strain (ϵ_{22}) and the maximum shear strain (γ_{max}) for specimen SBC-0-1 at the 95% peak load stage (post-peak regime) and for SBC-3.5-1 at the peak load stage. The minimum principal strains (ϵ_{22}) and the maximum shear strain (γ_{max}) are known to provide a qualitative estimate of the damage due to tensile and shear micro-cracks, respectively. It is clearly shown in Figure 5a-d that three FPZs (FPZ-1, FPZ-2, and FPZ-3), characterized by the strain localized zones, have been formed between two notches in both SBC specimens (SBC-0-1 and SBC-3.5-1). The FPZ-1 represents the formation of a vertical crack between two notches of both SBC specimens (SBC-0-1 and SBC-3.5-1). It is composed of both tensile (negative (−) principal strain representing tension) and shear micro-cracks, as shown by a strain localization in both principal strain (ϵ_{22}) and the maximum shear strain (γ_{max}) (Figures 5a-d). Therefore, FPZ-1 (main crack) in both specimens will transition into a mixed-mode I/II fracture. Additionally, the SBC specimens under confined conditions (SBC-3.5-1) underwent a larger amount of damage as compared to SBC specimens under unconfined conditions (SBC-0-1), as evident by higher strain concentration in the localized zones of the former case (Figures 5a-d). This can be attributed to the high level of confining pressure (σ_c=3.5 MPa) in SBC-3.5-1 suppressed large-scale tensile micro-cracking and thereby increased fracture resistance of ligament region between two notches. This also facilitated the generation of more micro-cracks under shear in SBC-3.5-1, as evident by the larger concentration of maximum shear strain (γ_{max}~4 to 6% in SBC-3.5-1) as compared to the SBC specimen under the unconfined state (γ_{max} ~ 0 to 2% in SBC-0-1) (Figures 5c-d). The remaining two FPZs (represented by FPZ-2 and FPZ-3 in Figures 5a-d) were initiated from the inner surfaces of two notches in both SBC specimens (SBC-0-1 and SBC-3.5-1) but didn't lead to failure of SBC specimens.

In this study, the displacement approach involving the analysis of full-field surface deformation was also analyzed to determine the fracture mode. According to LEFM, the fracture mode is defined based on the displacement profiles across the crack faces. For instance, a mode I crack (tensile crack) only has normal displacements across its faces (i.e., opening displacements), while a mode II crack (shear crack) has displacements parallel to the crack faces (i.e., sliding displacements). Similarly, mixed-mode I/II crack has both opening and sliding displacements across its faces.

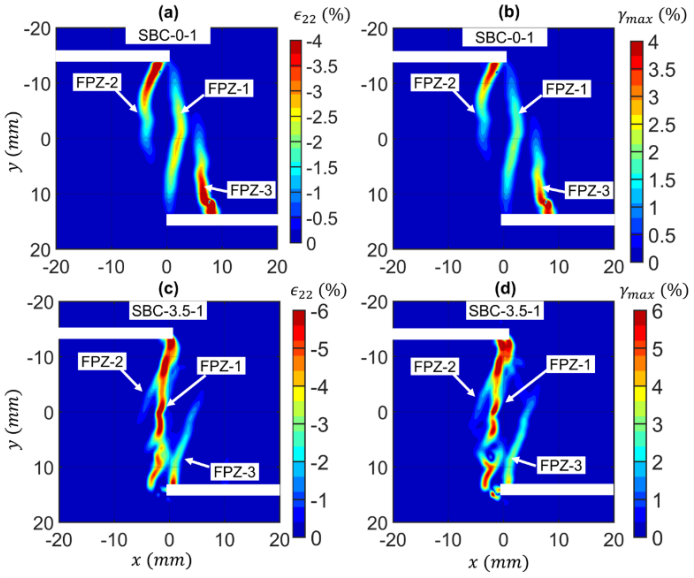

Figure 5: Contour of (a-c) minimum principal strain (ϵ_{22}) (b-d) and maximum shear strain (γ_{max}) obtained by 2D-DIC for SBC-0-1 at 95 % peak load (post-peak regime) and SBC-3.5-1 at peak load stage.

Figures 6a-d present the distribution of both horizontal (U) and vertical displacement (V) fields along with their profile across the three horizontal cross-sections (y =-5 mm, 0 mm, and 5 mm) at the 95% of the peak load (post-peak regime) for SBC specimen under unconfined state (SBC-0-1). The shaded region in Figures 6c-d represents the approximate width of three FPZs (FPZ-1, FPZ-2, and FPZ-3). The width of three FPZs was estimated based on the range of positive horizontal displacement gradient ($\partial U/\partial x$) in displacement profile along three cross-sections (y = -5 mm, 0 mm, and 5 mm in Figure 6c). The FPZ's width is a material property that represents the lateral size of the micro-cracking region (normal to crack path). Therefore, for each FPZ, a small region containing the positive horizontal displacement gradient ($\partial U/\partial x$) was selected (three shaded regions in Figure 6c). The selection of small FPZ width also ensured that the crack displacements only account for micro-cracking inside the given FPZ while minimizing the influence of other nearby FPZs. Additionally, the selection of the FPZ's width was made only based on horizontal displacement profiles and not the vertical displacement profiles (Figures 6c-d) as the former presents a more accurate estimation.

The contour of horizontal displacement (U) clearly shows the formation of three distinct FPZs (characterized by the merged displacement contours in figure 6a), similar to the contour of minimum principal strain (ϵ_{22}) (Figure 5a). This results in the formation of the three distinct regions of positive horizontal displacement gradient ($\partial U/\partial x$), as shown by horizontal displacement profiles along three cross-sections (y =-5 mm, 0 mm, and 5 mm) (Figure 6c). In contrast, the vertical displacement (V) field only indicates the formation of two FPZs (FPZ-1 and FPZ-3) (Figures 6b). The vertical displacement profiles along all three cross-sections (y =-5 mm, 0 mm, and 5 mm) indicated the formation of only one distinct region of positive vertical displacement gradient ($\partial V/\partial x$) (-6 mm < x < 6 mm in Figure 6d) but with a larger extent as compared to one obtained from horizontal displacement profile (0 mm < x < 4 mm in Figure 6c). This larger extent of positive vertical displacement gradient ($\partial V/\partial x$) (Figure 6d) can be attributed to the combination of various factors such as large elastic deformation, small sliding displacements along FPZ-1, and the formation of three FPZs in a narrow region. The material between two notches undergoes large elastic deformation in the vertical direction due to interaction between two notches (described in section 4.3). This along with the formation of three FPZs inside a small width (-4 mm < x < 8 mm in Figure 6a), resulted in a single region of positive displacement gradient ($\partial V/\partial x$) with a large width positive vertical displacement gradient ($\partial V/\partial x$) (Figure 6d). Therefore, the actual width of FPZ-1 is represented by the region of positive horizontal displacement gradient ($\partial U/\partial x$) (highlighted by the shaded region FPZ-1 in figure 6c). The FPZ-1 in SBC-0-1 transitions into a mixed-mode I/II macro-crack between two notches, as evidenced by a positive displacement gradient across its width in horizontal and vertical displacement profiles (Figure 6c-d).

Similarly, in the case of the SBC specimen under confined conditions (SBC-3.5-1), the formation of the three FPZs in a small width (-5 mm < x < 5 mm in Figure 5c) yielded two distinct regions of merged contours in horizontal and vertical displacement fields at peak load stage (Figure 7a-b). Consequently, both horizontal and vertical displacement profiles along three cross-sections (y =-5 mm, 0 mm, and 5 mm) only showed the two distinct regions of the positive displacement gradient (shaded regions in Figures 7c-d) representing the formation of FPZ-1 and FPZ-3. The FPZ-1 in SBC-3.5-1 also transitions to a vertical macro-crack between two notches (Figures 7a and 7c) involving both tensile and shear components, as evident by a large positive gradient in horizontal and vertical displacement profiles (shaded regions in Figures 7c-d). The width of FPZ-1 in this SBC specimen can be again represented by the small region of positive horizontal displacement gradient ($\partial U/\partial x$) (shown by the shaded region FPZ-1 in figure 7c).

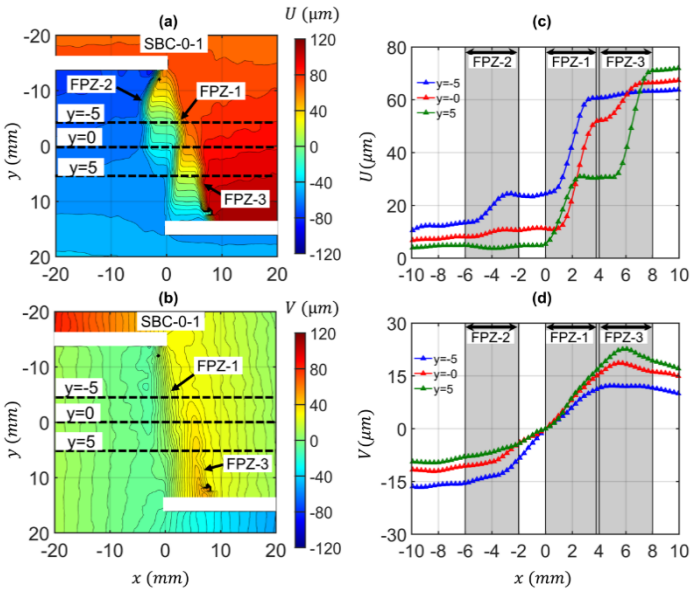

Figure 6. Specimen SBC-0-1, at 95% peak load (post-peak regime): Contours of (a) horizontal displacement; (b) vertical displacement; three horizontal cross-sections, i.e., y = -5mm, 0 mm, 5 mm showing (c) plot of horizontal displacement (U) profiles (d) plot of vertical displacement (V) profiles.

In most of the tested SBC specimens, the dominant fracture that resulted in specimen failure was initiated at the location of the FPZ-1. Therefore, the remainder of the study mainly focuses on the fracture process occurring inside the FPZ-1. Since the multiple FPZs in both SBC specimens (SBC-0-1 and SBC-3.5-1) are confined in a narrow region, it is vital to separate the influence of FPZ-1 from other FPZs to ensure accurate estimation of crack opening and sliding displacements. This is done by selecting a small width only containing the positive horizontal displacement gradient ($\partial U/\partial x$) around FPZ-1 (represented by the shaded region FPZ-1 in Figures 6c and 7c) in both SBC specimens. Therefore, the normal and tangential displacements field along the FPZ-1 were calculated as relative differences of the horizontal and vertical displacements (U, V) across its width (represented by the shaded region FPZ-1 in Figures 6c and 7c) in the two SBC specimens. Additionally, the central portion of ligament length (-5mm < y <5 mm) mostly has FPZ-1, as seen in the contour of minimum principal strain (ϵ_{22}) in both SBC specimens. Therefore, the FPZ evolution of the central portion of ligament length (-5mm < y <5 mm) was analyzed in the next section.

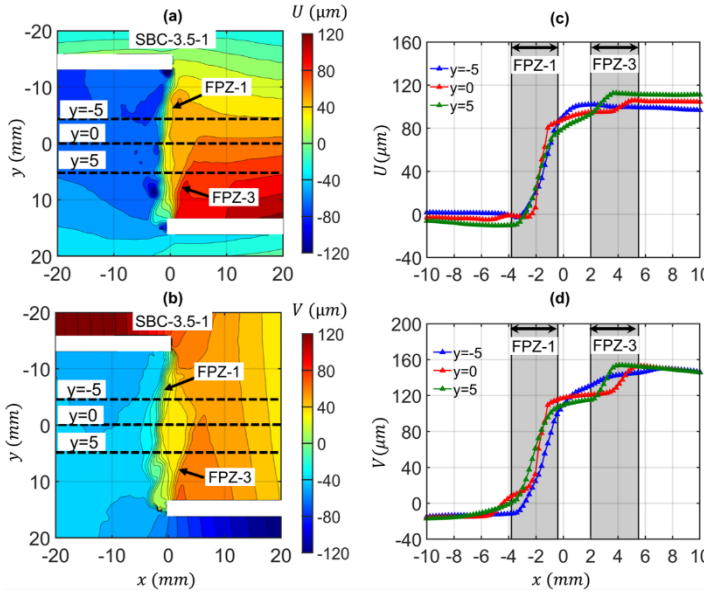

Figure 7. Specimen SBC-3.5-1, at peak load stage: Contours of (a) horizontal displacement; (b) vertical displacement; three horizontal cross-sections, i.e., y = -5mm, 0 mm, 5 mm showing (c) plot of horizontal displacement (U) profiles (d) plot of vertical displacement (V) profiles.

4.3 FPZ evolution using 2D-DIC analysis

This section presents the evolution of the fracture process inside the FPZ-1 in the SBC specimens. As discussed in section 4.2, only a central portion along ligament length (-5 mm < y < 5 mm) between two notches should be used as it mainly contains a single micro-cracking zone (FPZ-1). Therefore, the evolution of horizontal and vertical displacement profiles along a central cross-section of y=0 mm was analyzed for both SBC specimens (SBC-0-1 and SBC-3.5-1).

Figures 8a-d present the horizontal and vertical displacement profiles along the central cross-sections of y=0 mm at the various loading stages for two SBC specimens (SBC-0-1 and SBC-3.5-1). At the initial loading stages, both horizontal and vertical fields showed a linear displacement profile (Figures 8a-d), signifying an elastic deformation at this location in both SBC specimens (SBC-0-1 and SBC-3.5-1). Additionally, vertical displacement profiles showed a large gradient under elastic deformation (Figures 8c-d), which resulted in a non-negligible crack sliding displacement across the width of FPZ-1 in both SBC specimens (SBC-0-1 and SBC-3.5-1). For instance, crack sliding displacement of 3 µm, and 10 µm were observed in SBC-0-1 and SBC-3.5-1 at 70% peak load (pre-peak regime), respectively (Figures 8c-d). This large gradient in vertical displacement profiles can be attributed to the interaction between two horizontal notches, resulting in large vertical deformation in the ligament region. With additional loading, both horizontal and vertical fields showed a nonlinear displacement profile (Figure 8a-d) in two SBC specimens (SBC-0-1 and SBC-3.5-1), signifying the formation of FPZ at the location. Therefore, the crack displacements characterizing the FPZ formation should only account for nonlinear portions of displacement profiles. For this purpose, total crack opening (w_t^n) and sliding displacements (w_t^s) were calculated first based on the methodology described in section 4.2. This is followed by the calculation of the inelastic component of crack displacements as given by:

$$w_{ne}^n = w_t^n - w_e^n \quad (2a)$$

$$w_{ne}^s = w_t^s - w_e^s \quad (2b)$$

where w_{ne}^n and w_{ne}^s represent the inelastic components of crack opening and sliding displacement, respectively. The elastic component of crack opening (w_e^n) and sliding displacements (w_e^s) were calculated based on the FPZ initiation stage at this location. The FPZ initiation at the central cross-section of y=0 mm occurred around peak load and 70% of peak load (pre-peak regime) in specimens SBC-0-1 and SBC-3.5-1, respectively, as evident by an approximate linear profile of horizontal displacement for these specimens (Figures 8a-b). Based on this methodology, the elastic crack opening displacement (w_{ne}^n) was around 2 µm and 5.6 µm for SBC-0-1 and SBC-3.5-1, respectively. In a similar manner, elastic crack sliding displacement (w_{ne}^s) was estimated and is approximately equal to 4.5 µm and 10 µm for SBC-0-1 and SBC-3.5-1, respectively.

Figure 9a-b presents the evolution of the inelastic component of crack opening (w_{ne}^n) and sliding displacement (w_{ne}^s) inside FPZ-1 with respect to the normalized load-point displacement (δ_{norm}) for two SBC specimens (SBC-0-1 and SBC-3.5-1). The FPZ initiation occurred approximately at peak load and 70% of peak load (pre-peak regime) in specimen SBC-0-1 and SBC-3.5-1, respectively (represented by point A in Figures 9a-b), as evident by non-zero values of inelastic crack displacements from this point. With further loading, both crack opening (w_{ne}^n) and sliding displacement (w_{ne}^s) increased with an accelerated rate (Figures 9a-b) in both SBC specimens (SBC-0-1 and SBC-3.5-1) and consequently had a rapid jump in the post-peak regime. The onset of the rapid jump in the crack opening (w_{ne}^n) and sliding displacement (w_{ne}^s) signifies the occurrence of unstable crack propagation (represented by point B in Figure 9a-b), which also leads to the failure of SBC specimens.

In the study, the influence of confinement on the SBC specimens was assessed by analyzing the evolution of crack opening (w_{ne}^n) and sliding displacements (w_{ne}^s) inside the FPZ-1 (Figures 9a-b). The FPZ-1 in the SBC specimen under an unconfined state (SBC-0-1) is

characterized by an equal amount of mode I and mode II components, as evident by similar values of inelastic crack opening (w_{ne}^{n}) and sliding displacement (w_{ne}^{s}) (Figure 9a) while FPZ-1 in the SBC specimen under a confined state (SBC-3.5-1) involves a large magnitude of mode II components after the peak load stage. This can be attributed to the significant amount of confining pressure in SBC-3.5-1 (P = 3.5 MPa) that resulted in the suppression of tensile micro-cracking and, consequently, facilitated the generations of more micro-cracks under shear. Additionally, the confining pressure in SBC-3.5-1 also resulted in a significantly larger damage level as compared to SBC-0-1 inside the FPZ-1, as evident by large values of crack displacements (w_{ne}^{s} and w_{ne}^{n}) at the onset of unstable crack propagation in the former case. A similar observation of larger mode II components was observed in the SBC specimens at other confining pressure (P =10.4 MPa), as shown in Table 1. Table 1 presents values of crack opening (w_{ne}^{n}) and sliding displacements (w_{ne}^{s}) inside FPZ-1 at the onset of unstable crack propagation in SBC specimens under various levels of confining pressure (P =0, 1.7, 3.5, 10.4 MPa). It can be concluded that the FPZ-1 will transition into a mixed-mode I/II vertical fracture formed between two notches in all SBC specimens.

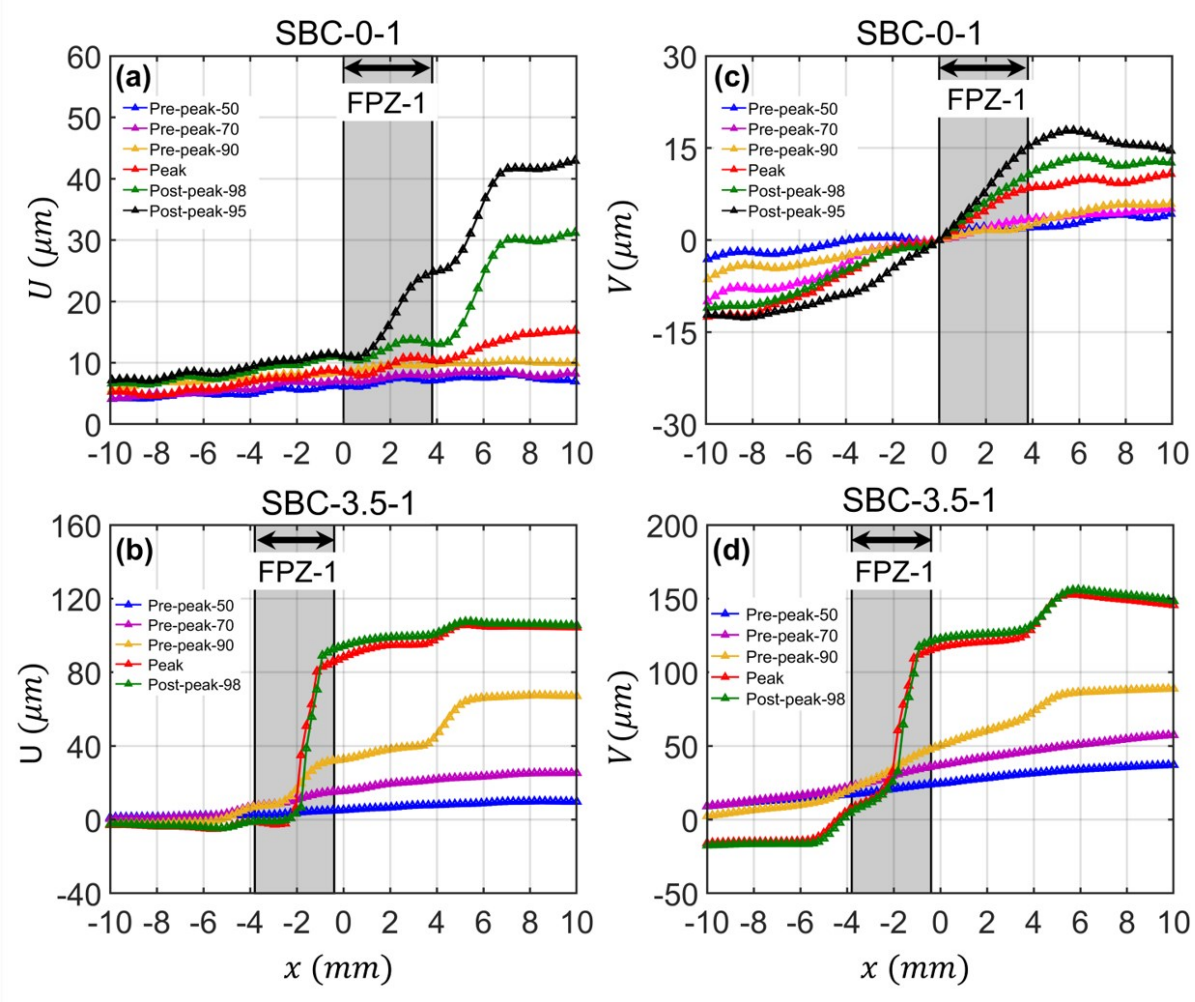

Figure 8. Plot of (a-b) horizontal displacement (U) profiles (c-d) and vertical displacement (V) profiles along the central cross-section of y = 0 mm at various loading stages for two SBC specimens (SBC-0-1 and SBC-3.5-1).

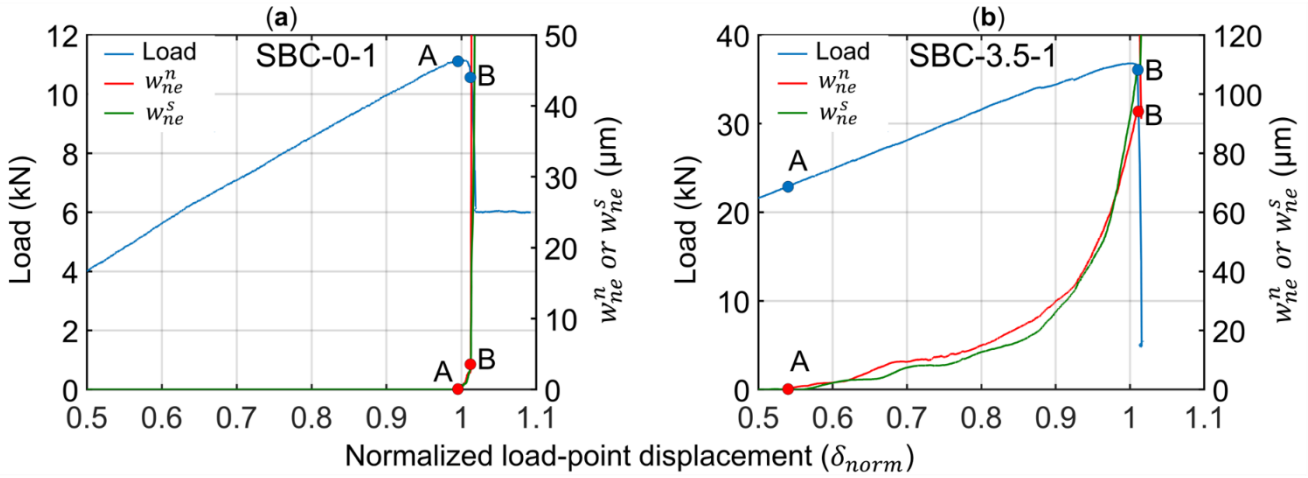

Figure 9(a-b) Variation of load, the inelastic component of COD and CSD for FPZ-1 with the applied load-point displacement in two SBC specimens (SBC-0-1 and SBC-3.5-1).

5. CONCLUSION

The short beam compression tests on Barre granite specimens were performed to characterize the development of the FPZ under pure mode II loading. Various crack characteristics such as fracture mode and its location were identified using the DIC imaging. Additionally, the SBC specimens were also tested under multiple levels of confining pressure (P =0, 1.7, 3.5, 10.4 MPa). The major findings are as follows:

1. Mode II fracture toughness was obtained using FEM analysis. It was found to increase linearly with increasing levels of confining pressures.

2. In all tested SBC specimens, failure occurred due to the formation of a vertical fracture between two notches. The DIC-based analysis characterized it as a mixed-mode I/II crack, irrespective of confining pressure applied to the SBC specimens.

3. The influence of confinement on the SBC specimens was assessed by analyzing the evolution of crack opening (w_{ne}^n) and sliding displacements (w_{ne}^s) inside the FPZ-1 that subsequently transitions into the vertical fracture between two notches.

4. The FPZ-1 in the SBC specimen under the unconfined state is characterized by an equal amount of mode I and mode II components. In contrast, the FPZ-1 in the SBC specimen under a confined state involves a large magnitude of mode II components after the peak load stage

5. Larger levels of damage in confined specimens were observed before the failure than in the unconfined specimens, as evident by significantly higher magnitudes of crack displacements at the onset of unstable crack propagation. This indicated an increase in the fracture resistance and therefore mode II fracture toughness with the confining stress.

ACKNOWLEDGEMENTS

Funding for this research was provided by the National Science Foundation under award number 1644326. The authors are grateful for this support.

REFERENCES

1. Aliha MRM, Ashtari R, Ayatollahi MR. (2006). Mode I and Mode II Fracture Toughness Testing for a Coarse Grain Marble. Applied Mechanics and Materials;5–6:181–8.

2. Ayatollahi MR, Sistaninia M. (2011). Mode II fracture study of rocks using Brazilian disk specimens. International Journal of Rock Mechanics and Mining Sciences;48:819–26.

3. Backers T, Stanchits S, Dresen G. (2005). Tensile fracture propagation and acoustic emission activity in sandstone: The effect of loading rate. International Journal of Rock Mechanics and Mining Sciences;42:1094–101.

4. Backers T, Stephansson O, Rybacki E. Rock fracture toughness testing in Mode II—punch-through shear test. Int J Rock Mech Min Sci 2002;39:755–69.

5. Backers T. 2004. Fracture Toughness Determination and Micromechanics of Rock Under Mode I and Mode II Loading. Doctoral Thesis, University of Potsdam, Germany.

6. Garg P, Hedayat A, Griffiths DV (2021). Investigation of Fracture Process Zone in Barre Granite under Mode II Loading. In: 55th U.S. Rock Mechanics/Geomechanics Symposium.

7. Garg P, Shirole D, Hedayat A, Griffiths DV (2020a). Numerical simulation of fracture initiation in Barre Granite using an experimentally validated XFEM

model. In: 54rd U.S. Rock Mechanics/Geomechanics Symposium.

8. Garg, P., Hedayat, A., and Griffiths, D.V. (2020b). Characterization of fracture process zone using surface deformation and strain field in brittle rocks. Rock Mechanics and Rock Engineering (under review).
9. Ghamgosar M, Erarslan N. (2016). Experimental and Numerical Studies on Development of Fracture Process Zone (FPZ) in Rocks under Cyclic and Static Loadings. Rock Mechanics and Rock Engineering;49:893–908.
10. Hedayat A, Pyrak-Nolte LJ, Bobet A. (2014). Multi-Modal Monitoring of Slip Along Frictional Discontinuities. Rock Mechanics and Rock Engineering;47:1575–87.
11. Ji WW, Pan PZ, Lin Q, Feng XT, Du MP. (2016). Do disk-type specimens generate a mode II fracture without confinement? International Journal of Rock Mechanics and Mining Sciences;87:48–54.
12. Ko, T.Y. 2008. Subcritical crack growth under mode I, II, and III loading for Coconino sandstone. Ph.D. dissertation. Tucson: University of Arizona
13. Ko, T.Y., Kemeny, J., 2007. Effect of Confining Stress And Loading Rate On Fracture Toughness of Rocks, in: 1st Canada - U.S. Rock Mechanic Symposium, American Rock Mechanics Association, Vancouver, Canada. p. 5.
14. Li BQ, Einstein HH. (2017). Comparison of Visual and Acoustic Emission Observations in a Four Point Bending Experiment on Barre Granite. Rock Mechanics and Rock Engineering;50:2277–96.
15. Li, D, Zhang, C, Zhu, Q, Ma, J, Gao, F. Deformation and fracture behavior of granite by the short core in compression method with 3D digital image correlation. Fatigue Fract Eng Mater Struct. 2022; 45(2): 425- 440. doi:10.1111/ffe.13606.
16. Lin Q, Ji WW, Pan PZ, Wang S, Lu Y. (2019). Comments on the mode II fracture from disk-type specimens for rock-type materials. Engineering Fracture Mechanics;211:303–20.
17. Lin Q, Wang S, Pan PZ, Ji WW, Lu Y. (2020). Fracture initiation under pure shear revisited: Remarks on the mode II fracture in quasi-brittle materials. Theoretical and Applied Fracture Mechanics;109.
18. Liu HZ, Lin JS, He J da, Xie HQ. (2018). Dominant mode of planar fractures and the role of material properties. Engineering Fracture Mechanics;195:57–79.
19. Luo Y, Ren L, Xie LZ, Ai T, He B. (2017). Fracture Behavior Investigation of a Typical Sandstone Under Mixed-Mode I/II Loading Using the Notched Deep Beam Bending Method. Rock Mechanics and Rock Engineering;50:1987–2005.
20. Miao S, Pan PZ, Yu P, Zhao S, Shao C. (2020). Fracture analysis of Beishan granite after high-temperature treatment using digital image correlation. Engineering Fracture Mechanics;225.
21. Mirsayar MM, Razmi A, Aliha MRM, Berto F. (2018). EMTSN criterion for evaluating mixed mode I/II crack propagation in rock materials. Engineering Fracture Mechanics;190:186–97.
22. Sharafisafa M, Shen L, Xu Q. (2018). Characterisation of mechanical behaviour of 3D printed rock-like material with digital image correlation. International Journal of Rock Mechanics and Mining Sciences;112:122–38.
23. Shirole D, Walton G, Hedayat A. (2020). Experimental investigation of multi-scale strain-field heterogeneity in rocks. International Journal of Rock Mechanics and Mining Sciences;127.
24. Wang C, Zhu ZM, Liu HJ. On the I-II mixed mode fracture of granite using four-point bend specimen. Fatigue Fract Eng Mater Struct. 2016;39(10):1193-1203.
25. Watkins J, Liu K. A finite element study of the short beam test specimen under mode II loading. Int J Cem Compos Lightweight Concrete. 1985;7(1):39-47.
26. Xu Y, Yao W, Zhao GL, Xia KW. Evaluation of the short core in compression (SCC) method for measuring mode II fracture toughness of rocks. Eng Fract Mech. 2020;224:106747.